

Proceedings of the ASME 2020
International Design Engineering Technical Conferences
and Computers and Information in Engineering Conference
IDETC/CIE2020
August 17-19, 2020, Virtual, Online

DETC2020-22551

DEPLOYABLE CONVEX GENERALIZED CYLINDRICAL SURFACES USING TORSIONAL JOINTS

Todd G Nelson*

Department of Engineering University of Southern Indiana Evansville, Indiana 47712 Email: tgnelson@usi.edu

Zhicheng Deng

School of Aeronautic Science and Engineering Beijing University of Aeronautics & Astronautics Beijing, 100191, China

Luis M. Baldelomar Pinto

Department of Engineering University of Southern Indiana Evansville, Indiana 47712

Curtis G Nelson

Department of Mathematics Brigham Young University - Idaho Rexburg, Idaho 83460

Jared T. Bruton

Compliant Mechanisms Research Group Department of Mechanical Engineering Brigham Young University Provo, Utah 84604

Larry L. Howell

Compliant Mechanisms Research Group
Department of Mechanical Engineering
Brigham Young University
Provo. Utah 84604

ABSTRACT

The ability to deploy a planar surface to a desired convex profile can enhance foldable or morphing airfoils, deployable antennae and reflectors, and other applications where a specific profile geometry is desired from a planar sheet. A model using a system of rigid links joined by torsional springs of tailorable stiffness is employed to create an approximate curved surface when two opposing tip loads are applied. The physical implementation of the model uses compliant torsion bars as the torsion springs. A multidimensional optimization algorithm is presented to minimize the error from the rigid-link approximation and account for additional manufacturing and stress considerations in the torsion bars. A proof is presented to show that equal torsion spring spacing along the horizontal axis of deployed parabolic profiles will result in minimizing the area between the model's rigid-link approximation and smooth curve. The model is demonstrated through the physical construction of a deployable airfoil surface and a metallic deployable parabolic reflector.

1 Introduction

The objective of this research is to present a model which can be used to create a deployable surface that closely approximates a generalized cylindrical surface, such as the one shown in Fig. 1. The ability to transition from a flat sheet to a predetermined shape can lead to advances in applications such as stowable reflectors incorporated in space mechanisms, tunable optical devices, morphing aerodynamic or hydrodynamic structures, and conforming components like circuit boards to curved shapes.

A generalized cylindrical surface is one of the three classes of curved developable surfaces. A developable surface can be formed from a planar surface through bending without any stretching or tearing [1]. A generalized cylinder is formed by translating a straight line, called the generator line, along a path in a plane perpendicular to the generator line. The path is called the directrix of the generalized cylinder. For example, a circular directrix would give rise to the common right circular cylinder. The model presented in this research enables the design of deployable, approximate generalized cylindrical surfaces where the

^{*}Address all correspondence to this author.

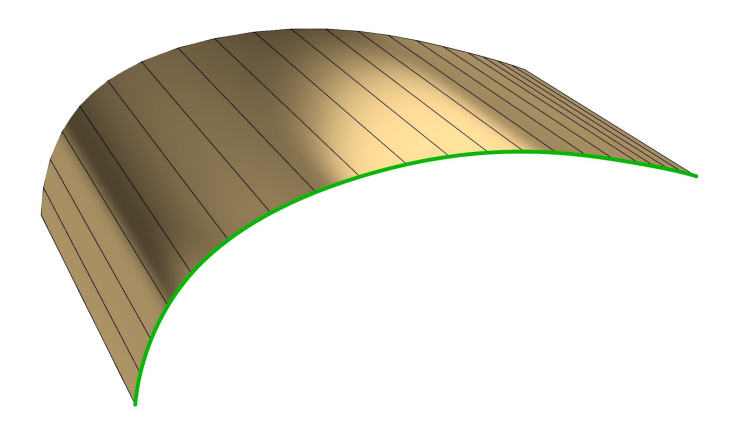


FIGURE 1. A generalized cylinder with ruling lines (black) and a convex directrix (green).

directrix is a convex curve that does not self-intersect. Furthermore, the model is extended through optimization techniques to minimize error in the approximation of the surface and to include constraints on various parameters to ensure the functionality and manufacturability of the surface.

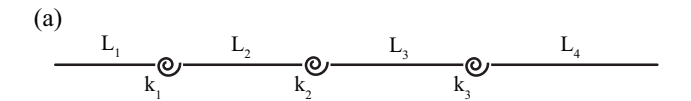
Surfaces which can be controlled or predictably changed offer advantages in situations where a change in occupied space or a dynamic response to an environment is desired [2-5]. Origami and origami-inspired mechanisms provide examples of surfaces where a change from one state, perhaps a tightly compacted state, to another state, a deployed state, is desired. Examples of these include bio-inspired wing structures [6], a diameter-changing origami wheel [7], and an origami-based heart stent [8]. Morphing wings and flight surfaces have also been investigated to create structures which can be dynamically modified to achieve geometries which perform well under varying environments or conditions [9–13]. Deployable reflectors also use the principle of morphing or changing surfaces to create the desired collection shape while still having the ability to stow compactly [14–18]. Optimization is commonly employed to assist in the determination of geometry for morphing geometries [19, 20].

This work specifically looks at generalized cylindrical surfaces, which are one of the four possible developable surfaces resulting from curved folds or creases in a surface [1]. The results of this work could possibly be incorporated into mechanisms and structures derived from curved-fold origami patterns to facilitate specific panel shapes or further increase the propensity of a panel to take a certain shape during deployment [21].

2 Method

2.1 Spring and Rigid-link Model for Generalized Cylindrical Deployable Surfaces

A model for creating generalized cylindrical deployable surfaces uses a system of rigid links joined by torsional springs that



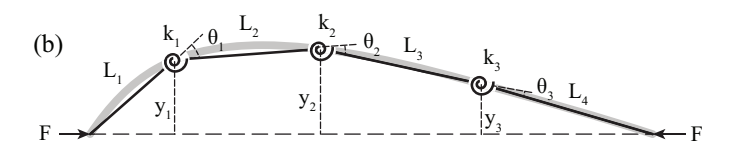


FIGURE 2. Rigid link and torsion spring model showing (a) a flat position and (b) an actuated position for a rigid-link system of N = 3.

is actuated from a flat state by opposing tip loads to form a desired directrix in a deployed state. The desired directrix is used to calculate the required stiffness of the torsional springs between each rigid link.

Let $L_1, L_2,...,L_{N+1}$ be the lengths of N+1 rigid links in the system and N is the number of joints between the links. Let $k_1,k_2,...,k_N$ denote the equivalent stiffness of the torsion springs between the rigid links as shown in Fig. 2(a). By placing the rigid-link system in the desired curved shape, represented by the function $y_{desired}(x)$, where all of the endpoints of the rigid links lie upon the curve, the deployed link angles $\theta_1, \theta_2,..., \theta_N$ and the deployed heights $y_1,y_2,...,y_N$, as shown in Fig. 2(b), can be determined. This can be accomplished using vectors that represent each of the links to calculate the angle between these vectors to obtain the deployed link angles, and using $y_{desired}(x)$ to find the deployed heights for each x corresponding to a joint location.

With the system of rigid links in the desired curved shape the moment at the i-th joint, M_i , can be expressed as

$$M_i = k_i \theta_i \tag{1}$$

The free body diagram drawn for the i-th joint in Fig. 3 with opposing tip loads, F, shows that the moment, M_i , can also be expressed as

$$M_i = F y_i \tag{2}$$

By equating Eq. 1 and 2 we can find an expression for the stiffness of each torsion spring in terms of known geometry as

$$k_i = \frac{Fy_i}{\theta_i} \tag{3}$$

The Lamina Emergent Torsion (LET) is a compliant joint that allows for a twisting motion [22–24]. A full LET joint consists of four torsion bars, a set of two parallel torsion bars (also

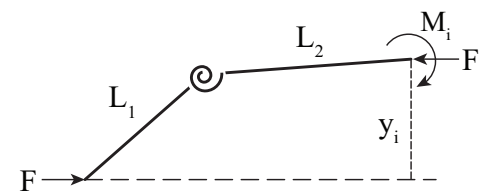


FIGURE 3. Free-body diagram of the structure cut at the *i*-th joint

called a torsional parallel joint [25]) in series with another set of two parallel torsion bars. LET joints can be chained together to form lines of torsion bars [21, 26]. The lines of parallel torsion bars can act as the torsion springs in the model. An example of the geometry of a LET joint chain with two torsion bars on each ruling line is detailed in Fig. 4. The torsion bars of the LET joints are well suited to the model for deployable surfaces as the joints can be planar manufactured as part of a sheet, have a relatively stable axis of rotation, and have geometry which can be modified to change the stiffness of the joint in a predictable way using a spring models [22,27]. For example, the length, width, or thickness of the torsion bars can be changed to specify a certain stiffness.

Chen et al. developed expressions for the stiffness of a rectangular torsion bar, the basic torsional element of the LET joint, that are symmetric (t and w are interchangeable) [28]. This is helpful for design situations where the geometry is not known a priori. The stiffness expression of a single rectangular bar is repeated here for reference [28]:

$$k = \frac{GJ}{L_t} \tag{4}$$

where G is the shear modulus of the material, L_t is the length of the torsion bar, and in terms of the width w and thickness of the torsion bar t

$$J = \left(\frac{2t^3w^3}{7t^2 + 7w^2}\right) \left(\frac{1.17t^2 + 2.191tw + 1.17w^2}{t^2 + 2.609tw + w^2}\right)$$
 (5)

The second grouped term in the expression for J can be replaced by a fifth degree polynomial for greater accuracy (see [28]) and this more accurate form of the equation was used in the implementation sections of this paper.

Because the value for the stiffness can be determined from the desired geometry with Eq. 3, this can be set equal to the expression for the stiffness of the torsion bar from Eqs. 4 and 5. Moreover, the expression from Eq. 4 is multiplied by a factor m which corresponds to the number of parallel torsion bars along the ruling line of the torsional spring k_i . Rearranging to move all

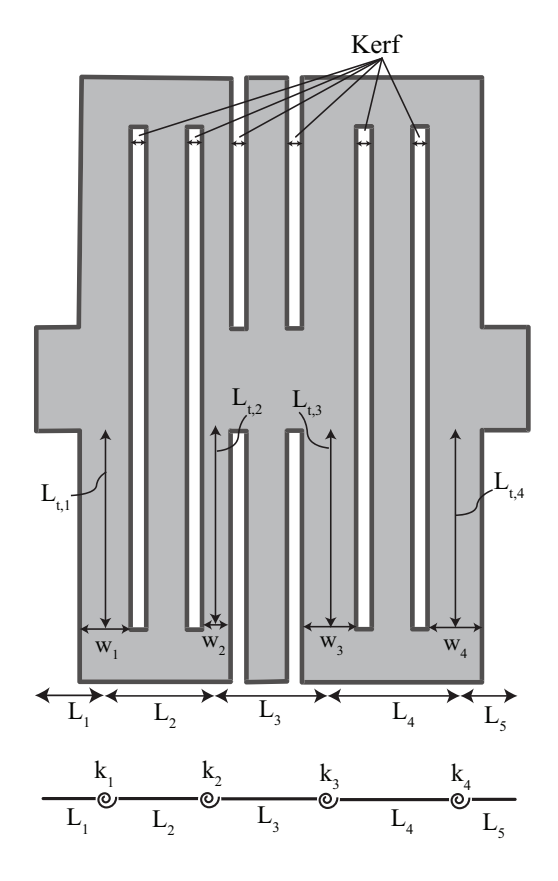


FIGURE 4. A chain of LET joints with important dimensions shown with the corresponding model schematic shown below. This chain has five rigid links and four torsion springs.

terms to a single side results for joint i,

$$0 = \frac{Fy_i}{\theta_i} - \frac{mGJ}{L_t} \tag{6}$$

There is some flexibility in determining which geometric parameter(s) are allowed to vary to satisfy this equation. For example, all terms could be defined except for *w* and the equation can be solved numerically to find the width of the torsion bar.

2.2 Joint Placement Optimization

Multidimensional optimization can be used to determine joint locations for a specified number of torsion joints, N, which will minimize the error in approximating the desired profile with a series of rigid links and allow for the introduction of additional constraints in the design problem.

The distances between joint locations, δ_i , are the design variables where i=1 to N. To simplify the optimization, problem constraints are added such that the design variables must be positive, represented as:

$$\delta_i > 0.$$
 (7)

These constraints ensure that the ordering of the torsion bars does not change through the optimization process. The design variables, δ_i , can be related to d_i , the distances of the torsion springs from one end of the deployed surface where i=1 to N as shown in Fig. 5.

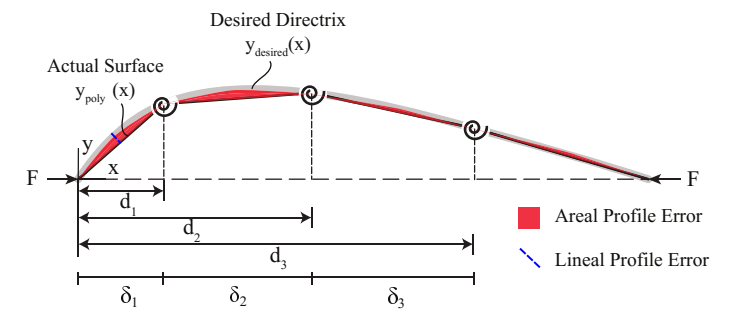


FIGURE 5. The design variables, δ_i , are the distances between torsional springs (three shown here). The objective to be minimized, the areal profile error between the desired and actual surface, is shown shaded in red. The lineal profile error which can be limited with a constraint is also shown.

The objective function for the optimization problem can be defined as a minimization of the *areal profile error*, the area between the desired directrix $y_{desired}(x)$ and the actual deployed shape's directrix $y_{poly}(x)$ where the subscript poly stands for polyline or polygonal chain. The objective function to be minimized is thus written as

$$F(\delta) = Areal \ Profile \ Error$$

$$= \int_{0}^{L} (y_{desired}(x) - y_{poly}(x)) \ dx$$
(8)

where $y_{poly}(x)$ is determined from the vector of design variables, δ_i , to create a piecewise function of straight lines representing the rigid links. During implementation numerical integration was used to evaluate the areal profile error.

It is best to pair this objective function with a constraint on the maximum deviation of the system from the desired curve, the *lineal profile error*. The lineal profile error can be expressed as

Lineal Profile Error

= max (shortest distance between $y_{desired}(x_{arb})$ and y_{poly}) (9)

where x_{arb} represents an arbitrary point along the desired curve. The constraint on this error's maximum allowable value is defined as

Lineal Profile Error \leq *Allowable Lineal Profile Error.* (10)

This prevents the shortest distance from an arbitrary point on $y_{desired}$ to y_{poly} from growing too large. If this constraint is not in place, the optimization process tends to aggregate all of the areal profile error to the location where the curvature of the desired function is the greatest, even if the distance from the desired curve to the actual deployed surface becomes large.

By imposing a limit on the maximum lineal profile error, the minimum areal profile error is increased, but distributed more evenly throughout the system. To gain an appropriate understanding of the range of this constraint the optimization can be performed with a large value for the allowable lineal profile error such that the constraint is not binding. The value of the constraint can then be reduced until it reaches at the other extreme a value which will cause the optimization problem to have no feasible solution.

In the implementation to evaluate this constraint, the lineal profile error was found by locating the largest lineal profile error for each segment described by δ_i . This was accomplished with another optimization routine where a single free variable, the x coordinate on $y_{desired}(x)$, was determined to maximize the objective function of the distance between the point $(x, y_{desired}(x))$ and the line segment (found using a form of the distance formula for the shortest length between a point and a line).

In addition to the lineal profile error constraint, to maintain a feasible geometry another constraint should limit the sum of the design variables to a value smaller than the maximum value of x for $y_{desired}$, that is

$$\sum_{i=1}^{N} \delta_i \le x_{\text{max}} \tag{11}$$

If desired, additional constraints can also be introduced such as the maximum angular rotation of a torsional spring and the minimum or maximum lengths of the rigid links. Once a mechanism, such as a torsion bar, is decided upon to serve as the torsion spring, further constraints can be imposed to limit stress or size of the mechanism.

To illustrate these additional constraints consider a rigid link system which uses N torsion springs, which corresponds to the number of design variables. Let's assume a geometry similar to the one shown in Fig. 4, where the number of torsion bars on each ruling line is two (m = 2) and the only geometric parameter we are allowing to change is the torsion bar widths w_i .

Several constraints can be added to ensure functionality and the ability to be manufactured for the torsional joint system. Constraints can be added to require each torsion bar width, w_i , to be greater than or equal to a minimum feasible width, $w_{min,allow}$, represented as

$$w_{min.allow} \le w_i \quad \text{for } i = 1 \dots N$$
 (12)

Constraints can be added to ensure the widths of the torsion bars of the torsion joints, w_i , fit into the dimensions for the link lengths, L_i , while accounting for the kerf from constructing the torsion joints. These constraints can be expressed as

$$\frac{\frac{w_1}{2} + \frac{kerf}{2} - L_1 \le 0}{\frac{w_{i-1}}{2} + \frac{w_i}{2} + kerf - L_i \le 0 \text{ for } i = 2...N}$$

$$\frac{\frac{w_N}{2} + \frac{kerf}{2} - L_{N+1} \le 0}{\frac{w_N}{2} + \frac{kerf}{2} - L_{N+1} \le 0}$$
(13)

The highest stress in any torsional bar with a displacement angle, θ_i , is a shear stress occurring in middle of the widest side of the torsion bar when stress concentrations are ignored. The highest shear stresses in each torsional bar, τ_i , can be constrained to be less than an allowable shear stress value, τ_{allow} .

$$\tau_i \le \tau_{allow}$$
 (14)

To calculate the highest shear stresses in each torsion bar a symmetric formula has been developed and can be used where t and w are once again interchangeable [29] as

$$\tau_i = \left(\frac{M_i(2.4w + 2.4t)}{w^2 t^2}\right) \left(\frac{1.271v^2 + 0.2829v + 0.0498}{v^2 + 0.27v + 0.0496}\right)$$
(15)

where $v = \left| \log \frac{t}{w} \right|$. Similar to Eq. 5, a more accurate higher order term is available for the second grouped term (see [29] for details) and this more accurate term was used in the implementation sections of this paper.

Scaling of the desired profile and constraints was used to increase the convergence rate for the optimization during implementation. For example the desired profile and allowable lineal profile error were scaled by a factor such that the maximum *x*-axis length of the desired profile was one, though care was taken to use the full-scale geometry when calculating dimensions such as widths, stresses, or the constraints in Eq. 13. Several constraints, such as Eq. 10, 12, and 14, were scaled by their allowable values.

2.2.1 Joint Placement for Parabolic Profiles During the implementation of the optimization algorithm for parabolic profiles it was noted that when the additional constraints for lineal profile error, stress, and manufacturing were not binding that the minimum areal profile error was achieved through equal δ_i spacing of the torsion springs. This can be shown mathematically as follows.

Proposition 1. Let f(x) be a function whose graph is a parabola on the interval $[\alpha, \beta]$. Let P be the polyline consisting of n line segments with endpoints, $(x_0 = \alpha, f(x_0))$, $(x_1, f(x_1))$, $(x_2, f(x_2)), \ldots, (x_{n-1}, f(x_{n-1}), (x_n = \beta, f(x_n))$. If P minimizes the areal profile error between itself and the parabola, then $x_{i+1} - x_i = \frac{\beta - \alpha}{n}$ for $i = 0, 1, \ldots, n-1$; i.e. the points are equally spaced along the x-axis.

Proof. Without loss of generality, we suppose that $\alpha = 0$ and that the parabola is above the x-axis on the interval $[0, \beta]$. The function f(x) can be written $f(x) = ax^2 + bx + c$ for some real numbers a, b and c. We give a proof by induction on n.

If n=2 then P consists of the points $(0,f(0)),(x_1,f(x_1))$, and $(\beta,f(\beta))$. Let T_1 denote the trapezoid formed from the points $(0,0),(0,f(0)),(x_1,f(x_1))$, and $(x_1,0)$. Let T_2 denote the trapezoid formed from the points $(x_1,0),(x_1,f(x_1)),(\beta,f(\beta))$ and $(\beta,0)$. Let $A(T_1)$ and $A(T_2)$ denote the areas of the two trapezoids respectively. The sum of these two areas can be expressed as as function of x_1 as follows

$$A(T_1) + A(T_2) = \frac{1}{2}(f(0) + f(x_1))x_1 + \frac{1}{2}(f(x_1) + f(\beta))(\beta - x_1)$$

$$= \frac{1}{2}(c + ax_1^2 + bx_1 + c)x_1$$

$$+ \frac{1}{2}(ax_1^2 + bx_1 + c + a\beta^2 + b\beta + c)(\beta - x_1)$$

$$= \frac{1}{2}(cx_1 + ax_1^3 + bx_1^2 + cx_1 + \beta ax_1^2 + \beta bx_1$$

$$+ \beta c + a\beta^3 + b\beta^2 + c\beta$$

$$- ax_1^3 - bx_1^2 - cx_1 - a\beta^2 x_1 - b\beta x_1 - cx_1)$$

$$= \frac{1}{2}(\beta ax_1^2 - \beta^2 ax_1 + \beta c + \beta^3 a + \beta^2 b + \beta c)$$

To maximize or minimize this function we take a derivative with respect to x_1 which results in $\frac{1}{2}(2\beta ax_1 - \beta^2 a)$. Setting this equal to 0 gives $x_1 = \frac{\beta}{2}$. The second derivate of the function is βa . Recall $\beta > 0$. Thus if a is negative, then the area function above is concave down and thus the function is maximized at $x_1 = \frac{\beta}{2}$. When a is negative, the parabola given by f(x) is also concave down. Thus, in this case, maximizing $A(T_1) + A(T_2)$ is equivalent to minimizing the areal profile error between P and

the parabola. If a is positive, then the second derivative of the area function is positive and thus the area function is minimized at $x_1 = \frac{\beta}{2}$. In this case the parabola is concave up and minimizing $A(T_1) + A(T_2)$ is equivalent to minimizing the areal profile error between P and the parabola. Therefore, in either case, the areal profile error between the parabola and P is minimized when x_1 is placed half way between a and b. This completes the base case.

Suppose the result holds when n = 1, 2, 3, ..., k for some integer k. Let P be a polyline consisting of k+1 line segments that minimizes the areal profile error. Consider the first k line segments. The x coordinates of the endpoints are $0, x_1, x_2, ..., x_k$. Note that the polyline consisting of these k line segments, call it P_k , must minimize the area profile error between P_k and the parabola given by f(x) on the interval $[\alpha, x_k]$. This is because if P_k did not minimize the areal profile error, then taking a polyline that did minimize this error and attaching the k+1 line segment from P would produce a polyline with a smaller areal profile error than P, a contradiction. Thus by the inductive hypothesis, $0, x_1, x_2, ..., x_k$ are equally spaced along the x-axis.

Now consider the last 2 line segments of P, line segments k and k+1. The x coordinates of the endpoints are x_{k-1}, x_k and $x_{k+1} = \beta$. By a similar argument as above, the polyline consisting of these line segments minimizes the areal profile error between itself and the parabola given by f(x) on the interval $[x_{k-1}, \beta]$. Thus by the inductive hypothesis, x_{k-1}, x_k and β are equally spaced along the x-axis.

Since the numbers in the overlapping lists $(0, x_1, x_2, \ldots, x_k)$ and (x_{k-1}, x_k, β) are equally spaced, the numbers in the list $(x_0, x_1, x_2, \ldots, x_k, \beta)$ are equally spaced. Therefore $x_{i+1} - x_i = \frac{\beta - \alpha}{k+1}$ for $i = 0, 1, 2, 3, \ldots, k$. This completes the inductive step and thus the result holds for all positive integers n.

3 Results

The methodology described above was used to create prototypes of a deployable airfoil surface and deployable parabolic reflector.

3.1 Deployable Airfoil Surface

A deployable airfoil surface was designed using torsion bars as the torsion springs in the model with optimization to place the joint locations and ensure constraints for the lineal profile error and for manufacturing were met. The desired directrix was chosen to be the top surface of a Clark Y airfoil with a 10 inch chord length [30]. The optimization and constraint set-up parameters are reported in Table 1.

After the optimization was completed the resulting LET joint pattern was cut from a polypropylene sheet using an abrasive waterjet. The pattern is shown in the flat and deployed states in Fig. 6. The optimization results and experimental measurements taken on the prototype are summarized in Table 2. Basic

TABLE 1. Optimization parameters for a deployable airfoil surface made from polypropylene.

Parameter	Value
Number of Torsion Springs (N)	12
Tip Load Force (F)	0.5 lb
Shear Modulus (G)	64.4 ksi
thickness of panel (t)	0.063 in
L_t	1.3 in
m	2
$W_{min,allow}$	0.06 in
kerf	1/16 in
$ au_{allow}$	1,590 psi
Allowable Lineal Profile Error	0.04 in

photogrammetry was carried out using MATLAB to measure approximate lineal profile error in the deployed shape. The largest error occurred in the leading edge where some parasitic or unwanted motion occurred due to compression of the LET joints by the tip loads. A thin PET adhesive film (2.5 mils thick) was then applied to the top layer of the pattern to decrease the parasitic motion while minimally affecting the torsion performance, similar to a technique investigated by Chen et al. [31]. This appeared to reduce some of the parasitic motion, yet increased the lineal profile error. The pattern with the PET covering is shown in Fig. 6(c).

The force to deploy the pattern to the profile was measured using a small digital scale. Accurate, repeatable measurements were limited with the current measurement set up and more rigorous instrumentation is recommended for future work. There is some discrepancy between the designed tip load force and the measured force. This could be due to a number of factors including errors in the shear modulus value used, manufactured kerf width, and perhaps most importantly bending observed from compressive forces in the structure that accompanied the torsional deflection.

3.2 Deployable Parabolic Reflector

The model was also used to design a deployable parabolic reflector made of Aluminum 7075-T6. The target deployed shape has a focal point four inches from the vertex. The flat, undeployed dimensions are 18.36 in by 10.2 in. The parameters used to set up the optimization are shown in Table 3. The resulting values after optimization and from experimental testing are de-

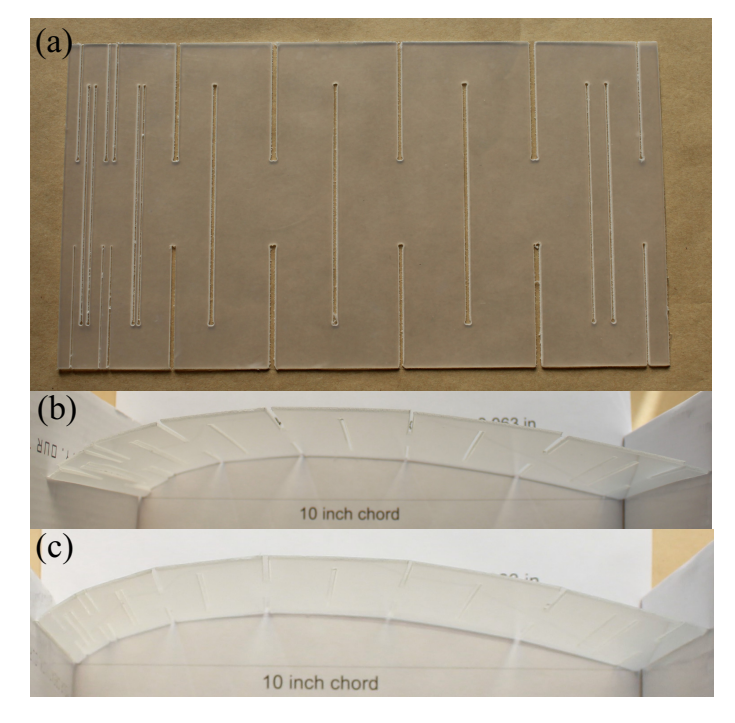


FIGURE 6. Deployable top surface of a Clark Y airfoil made from polypropylene using an abrasive water jet, where (a) is the flat surface, (b) is the deployed surface, and (c) is the deployed surface with a PET membrane to reduce parasitic motion.

scribed in Table 4. The optimized parabolic reflector was manufactured from the aluminum using a water jet and is shown in the flat and deployed states in Fig. 7.

The deployed profile and desired profile matched quite well with a small observed lineal profile error. However, once again a substantial discrepancy between the desired tip load force and the measured tip load force was observed. It is thought that similar to the polypropylene airfoil, bending unaccounted for in the torsion model, inaccuracies in material property estimates, and variations between the expected and actual kerf caused this discrepancy.

4 Discussion

Certain tradeoffs from employing torsion bars to create deployable surfaces can be illuminated by rearranging Eq. 6 as

$$(F)\left(\frac{1}{G}\right)\left(\frac{y_i}{\theta_i}\right) = \left(\frac{mJ}{L_t}\right) \tag{16}$$

From left to right these terms are determined by the desired actuation force, the material used, the desired profile curve, and on the right side of the equation all the factors in the term are

TABLE 2. Optimization and experimental results for a deployable airfoil surface made of polypropylene.

Parameters	Min value	Max Value
Deployed Spacing δ_i	0.181 in	1.142 in
Link Lengths, L_i	0.298 in	1.155 in
widths w_i	0.084 in	1.081 in
w_i/t ratios	1.33	17.16
Parameters from optimization results		Value
Lineal Profile Error		0.023 in
Areal Profile Error		0.0462 in^2
$ au_{max}$		795 psi
Shear stress factor of safety		2.004
Undeployed (Flat) length		10.315 in
Experimentally Measured Values		Value
Lineal Profile Error	(from Photogrammetry)	
without PET covering		≈ 0.036 in
with PET covering		≈ 0.057 in
Force to deploy to profile (from scale)		$0.35 \pm 0.1 \text{ lb}$

functions of the geometry of the torsion bar pattern. By grouping these terms we can see relationships such as if the geometry of a pattern is maintained (the right side of the equation), changing the material will scale the actuation force as long as the stresses do not exceed the new material's stress limit. Similarly, errors in estimating the value used for the shear modulus of a material should not affect the ability to achieve a desired profile shape as long as one is willing to adjust the actuation force to compensate for the modulus error.

It is also informative to look at an expression for the angular deflection of a torsion bar in terms of shear stress. Since a prescribed profile results in a displacement-limited design, rather than torque-limited design, the maximum stress in the system can be lessened by requiring smaller angular deflections and reducing the stiffness. Using Eqs. 1, 4, 5, and 15 we can write the angular deflection for a torsion bar as

$$\theta_i = \frac{\tau_i L_t}{G} f(t, w) \tag{17}$$

TABLE 3. Optimization parameters for a deployable parabolic surface made of aluminum.

Parameter	Value
Number of Torsion Springs (N)	22
Tip Load Force (F)	5.25 lb
Shear Modulus (G)	3,910 ksi
thickness of panel (t)	0.040 in
L_t	0.9 in
m	6
$W_{min,allow}$	0.1 in
kerf	1/16 in
$ au_{allow}$	38,800 psi
Allowable Lineal Profile Error	0.060 in

where f(t, w) is a function of t and w that depends on which form of J in Eq. 15 is selected (the higher order more accurate expression or expression presented in the equation). From this form we can see that there are several options to achieve the required deflections. The first is to reduce the required deflections θ_i themselves. This can be accomplished by increasing the number of torsion joints N which in turn lowers the θ_i magnitudes. The maximum number of joints N that can be introduced reaches a limit imposed by the manufacturing constraints that the widths of the torsion bars must fit within the link lengths. A second option to achieve required deflections is to choose a material with a high maximum shear stress to shear modulus ratio. Several materials and these ratios are shown in Table 5 to provide a comparison of how amenable a material is to large deflection of torsion bars. The third option to obtain the required deflections is to increase the torsion bar lengths, L_t . This can be limited by space constraints and also the introduction of unacceptable parasitic motions other than torsion when the torsion bar lengths are extended. Finally, t and w can be selected such that f(t, w) results in as large as values as possible. Chen et al. recommend a ratio of t/w to be ≤ 0.35 , = 1, or ≥ 2.86 to accomplish this [29].

Equation 16 implies that the number of torsion bars along a ruling line m can be changed to affect the magnitude of the tip load, yet m has no effect upon the stress, as m is not present and doesn't affect any of the terms in Eq. 17.

Minimizing the areal profile error in the model pushed all of the error between the desired and deployed directrix to the area of greatest curvature of the desired directrix. This was corrected by placing a constraint on the lineal profile error. The effect of

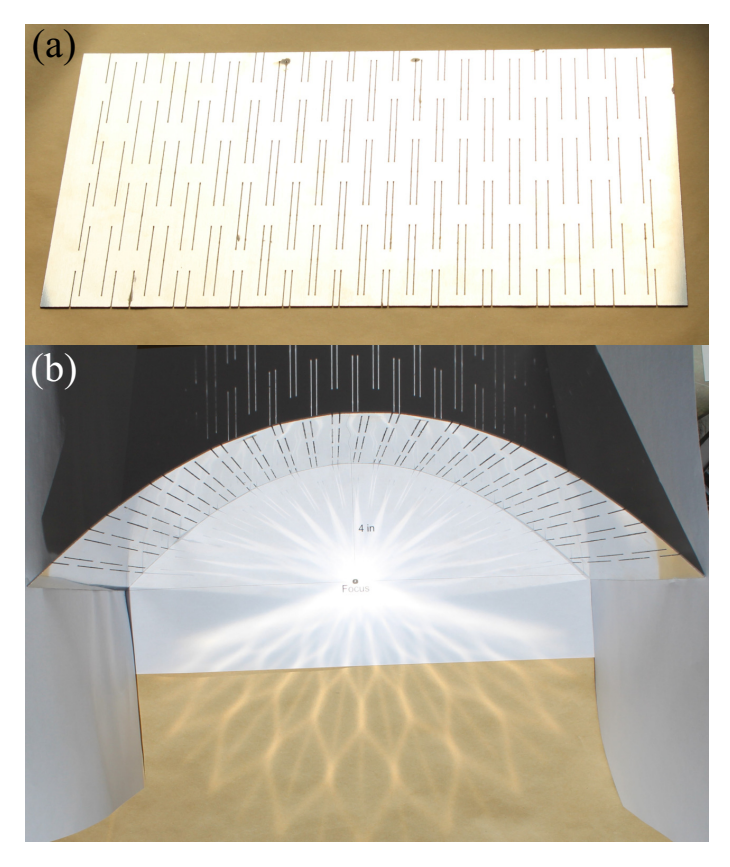


FIGURE 7. Deployable parabolic reflector made of aluminum, where (a) is the flat state, (b) is the deployed state with light reflecting off the surface.

minimizing the lineal profile error with a constraint on the areal profile error was also investigated with similar results, though the optimizer required more iterations to converge. Further investigation of definitions of profile error and suitable objective functions to minimize the error for the model present possible directions for future work.

As seen in the results from the physical prototypes, it appeared that bending accompanied the torsional deflection. Work can be done to incorporate bending effects into the analytical modeling for more accurate design estimates.

Both prototypes were deployed by moving two smooth barriers towards one another to create a compressive force. Tension elements, such as cables or strings, could be used to pull the two edges of the panel together to create an ultra-lightweight actuation method, though the effects of the point loads caused from the elements should be considered.

The model constructed using chains of torsion joints results in a deployable surface that can function as the final surface or as a structure underneath a flexible skin. Further studies need to be conducted to see how well the deployed surface would behave if used in an application with multiple loading conditions, such

TABLE 4. Optimization and experimental results for a deployable parabolic surface from aluminum.

Parameters	Min value	Max Value
Deployed Spacing δ_i	0.696 in	0.696 in
Link Lengths, L_i	0.696 in	0.963 in
widths w_i	0.158 in	0.460 in
w_i/t ratios	3.94	11.49
Parameters from optimization results		Value
Lineal Profile Error		0.008 in
Areal Profile Error		0.081 in^2
$ au_{max}$		15,070 psi
Shear stress factor of safety		2.57
Undeployed (Flat) length		18.361 in
Experimentally Measured Values		Value
Lineal Profile Error (from Photogrammetry)		≈ 0.018 in
Force to deploy to profile (from load cell)		$1.8 \pm 0.1 \text{ lb}$

as with a distributed pressure load from an aerodynamic loading. Because aerodynamic loads fluctuate, it poses a challenge to design a single structure for multiple load cases where both the deployed structure's stability and aerodynamic stability are considered. One possible path forward to address a more complex loading scenario would be to use a support structure underneath the deployed surface where hard stops align during deployment to resist compression loads on the surface of the structure.

5 Conclusion

A model has been presented as a way to create generalized cylindrical deployable surfaces with convex directrices conducive to being implemented with compliant joints. The model is demonstrated using the torsion bars of LET joints as torsion springs. A multidimensional optimization model was used to efficiently locate a given number of compliant joints along the directrix to minimize the error between the desired and actual directrix. Constraints were also enforced to ensure performance and a manufacturable geometry. The model was demonstrated through the physical creation of several prototypes in various materials. While the methodology shows potential for advancing the design of precise deployable surfaces, further investigation of

TABLE 5. A small sample of possible materials for torsion bars. Materials with high shear yield stresses, τ_{yield} to shear modulus ratios, G, are good candidates for maximizing deflection in deflection-limited torsion bar geometries (property values from supplier data sheets and [32], with approximations as required for shear modulus by G = E/(2(1+v)) and shear yield strength $\tau_{yield} \approx 0.577\sigma_{yield}$ where σ_{yield} is the tensile yield strength). *While PMMA has an excellent ratio, it is a brittle material and susceptible to stress concentrations.

Material	$1000 imes au_{yield}/G$
PMMA (Acrylic)	24.5*
Polypropylene	24.3
Titanium (Ti-6Al-4V)	11.7
Steel (4340)	11
Aluminum (7075-T6)	9.9

the effects bending accompanying the torsion and the effects of various loading conditions upon the deployed surfaces should be conducted. Actuation methods could also be incorporated into the material itself to create a compact package that can morph when a stimulus is applied.

ACKNOWLEDGMENT

This material is based on work supported by the National Science Foundation under NSF Grant 1663345 and NSF GRFP Grant 1247046. The authors acknowledge the University of Southern Indiana (USI) Foundation for supporting this research through a Science, Engineering, and Education Research Grant Award (SEERGA) and Justin Amos for his assistance with prototype fabrication. The authors would also like to acknowledge John Sinkovic for his insight into proving the optimal spacing for parabolic profiles where additional constraints were not binding.

REFERENCES

- [1] Struik, D. J., 1961. *Lectures on Classical Differential Geometry*, 2nd ed. Reading, Mass., Addison-Wesley Pub. Co.
- [2] Aoki, M., and Juang, J.-Y., 2018. "Forming three-dimensional closed shapes from two-dimensional soft ribbons by controlled buckling". *Royal Society Open Science*, 5(2), p. 171962.
- [3] Liu, L., Qiao, C., An, H., and Pasini, D., 2019. "Encoding kirigami bi-materials to morph on target in response to temperature". *Scientific Reports*, **9**(1), pp. 1–14.
- [4] Shaw, L. A., and Hopkins, J. B., 2016. "An actively con-

- trolled shape-morphing compliant microarchitectured material". *Journal of Mechanisms and Robotics*, **8**(2).
- [5] Peraza Hernandez, E. A., Hartl, D. J., Malak, R. J., Akleman, E., Gonen, O., and Kung, H.-W., 2016. "Design tools for patterned self-folding reconfigurable structures based on programmable active laminates". *Journal of Mechanisms and Robotics*, 8(3).
- [6] Faber, J. A., Arrieta, A. F., and Studart, A. R., 2018. "Bioin-spired spring origami". *Science*, 359(6382), pp. 1386–1391.
- [7] Lee, D.-Y., Jung, G.-P., Sin, M.-K., Ahn, S.-H., and Cho, K.-J., 2013. "Deformable wheel robot based on origami structure". In Robotics and Automation (ICRA), 2013 IEEE International Conference on, IEEE, pp. 5612–5617.
- [8] Kuribayashi, K., Tsuchiya, K., You, Z., Tomus, D., Umemoto, M., Ito, T., and Sasaki, M., 2006. "Self-deployable origami stent grafts as a biomedical application of Ni-rich TiNi shape memory alloy foil". *Materials Science and Engineering: A*, **419**(1), pp. 131–137.
- [9] Lentink, D., Müller, U., Stamhuis, E., De Kat, R., Van Gestel, W., Veldhuis, L., Henningsson, P., Hedenström, A., Videler, J. J., and Van Leeuwen, J. L., 2007. "How swifts control their glide performance with morphing wings". *Nature*, 446(7139), pp. 1082–1085.
- [10] Pettit, G. W., Robertshaw, H. H., and Inman, D. J., 2001. "Morphing wings for unmanned aircraft". *Smart Materials Bulletin*, **2001**(11), pp. 7–12.
- [11] Vasista, S., Tong, L., and Wong, K., 2012. "Realization of morphing wings: a multidisciplinary challenge". *Journal of Aircraft*, **49**(1), pp. 11–28.
- [12] Wang, H. V., and Rosen, D. W., 2006. "An automated design synthesis method for compliant mechanisms with application to morphing wings". In ASME 2006 IDETC/CIE Conference, ASME, pp. 231–239.
- [13] Yokozeki, T., Takeda, S.-i., Ogasawara, T., and Ishikawa, T., 2006. "Mechanical properties of corrugated composites for candidate materials of flexible wing structures". *Composites Part A: Applied Science and Manufacturing*, 37(10), pp. 1578–1586.
- [14] Thomson, M. W., 1999. "The astromesh deployable reflector". In Antennas and Propagation Society International Symposium, 1999. IEEE, Vol. 3, IEEE, pp. 1516–1519.
- [15] Stern, I., 2003. Deployable reflector antenna with tensegrity support architecture and associated methods, Apr. 1. US Patent 6,542,132.
- [16] Tan, L. T., and Pellegrino, S., 2004. "Ultra thin deployable reflector antennas". In Proc. 45th AIAA/ASME/ASCE/AHS/ASC Structures, Structural Dynamics and Materials Conference, pp. 19–22.
- [17] Kaplan, R., and Schultz, J. L., 1977. Deployable reflector structure, June 14. US Patent 4,030,102.
- [18] Freeland, R., Bilyeu, G., and Veal, G., 1995. "Valida-

- tion of a unique concept for a low-cost, lightweight space-deployable antenna structure". *Acta Astronautica*, **35**(9), pp. 565–572.
- [19] Funke, L. W., and Schmiedeler, J. P., 2017. "Simultaneous topological and dimensional synthesis of planar morphing mechanisms". *Journal of Mechanisms and Robotics*, 9(2).
- [20] Zhao, K., Schmiedeler, J. P., and Murray, A. P., 2012. "Design of planar, shape-changing rigid-body mechanisms for morphing aircraft wings". *Journal of mechanisms and robotics*, 4(4).
- [21] Nelson, T. G., Lang, R. J., Pehrson, N. A., Magleby, S. P., and Howell, L. L., 2016. "Facilitating deployable mechanisms and structures via developable lamina emergent arrays". *Journal of Mechanisms and Robotics*, 8(3), March, pp. 031006–031006–10.
- [22] Jacobsen, J. O., Chen, G., Howell, L. L., and Magleby, S. P., 2009. "Lamina emergent torsional (LET) joint". *Mechanism and Machine Theory*, 44(11), pp. 2098–2109.
- [23] Xie, Z., Qiu, L., and Yang, D., 2017. "Design and analysis of outside-deployed lamina emergent joint (od-lej)". *Mechanism and Machine Theory*, *114*, pp. 111–124.
- [24] Xie, Z., Qiu, L., and Yang, D., 2018. "Design and analysis of a variable stiffness inside-deployed lamina emergent joint". *Mechanism and Machine Theory,* 120, pp. 166–177.
- [25] Delimont, I. L., Magleby, S. P., and Howell, L. L., 2015. "A family of dual-segment compliant joints suitable for use as surrogate folds". *Journal of Mechanical Design*, *137*(9), p. 092302.
- [26] Nelson, T. G., Bruton, J. T., Rieske, N. E., Walton, M. P., Fullwood, D. T., and Howell, L. L., 2016. "Material selection shape factors for compliant arrays in bending". *Materials & Design*, 110, pp. 865 – 877.
- [27] Pehrson, N. A., Bilancia, P., Magleby, S. P., and Howell, L. L., 2020. "Load-Displacement Characterization in Three Degrees of Freedom for General LET Arrays". *Journal of Mechanical Design*, 01, pp. 1–22.
- [28] Chen, G., and Howell, L. L., 2009. "Two general solutions of torsional compliance for variable rectangular cross-section hinges in compliant mechanisms". *Precision Engineering*, *33*(3), pp. 268–274.
- [29] Chen, G.-M., and Howell, L. L., 2018. "Symmetric equations for evaluating maximum torsion stress of rectangular beams in compliant mechanisms". *Chinese Journal of Mechanical Engineering*, 31(1), p. 14.
- [30] Selig, M., 2020. UIUC airfoil data site, Univeristy of Illinois Department of Aerospace Engineering. https://m-selig.ae.illinois.edu/ads/coord_database.html.
- [31] Chen, G., Magleby, S. P., and Howell, L. L., 2018. "Membrane-enhanced lamina emergent torsional joints for surrogate folds". *Journal of Mechanical Design*, *140*(6).
- [32] Callister, W. D., and Rethwisch, D. G., 2018. *Materials science and engineering: an introduction*. Wiley New York.